

To appear on the February 1999 issue of the *The Astronomical Journal*

Quasar Candidates in the Hubble Deep Field¹

Alberto Conti, Julia D. Kennefick², Paul Martini, Patrick S. Osmer
Department of Astronomy, The Ohio State University,
Columbus, OH, 43210, USA.
conti, martini, osmer@astronomy.ohio-state.edu, julia@astro.ox.ac.uk

Abstract

The Hubble Deep Field gives us an unprecedented view of our universe and an opportunity to study a wide range of questions in galaxy evolution and cosmology. Here we focus on the search for unresolved faint quasars and AGN in the crude combine images using a multicolor imaging analysis that has proven very successful in recent years. Quasar selection was carried out both in multicolor space and in “profile space”. The latter is the multi-parameter space formed by the radial profiles of the objects in the different images. By combining the dither frames available for each filter, we were able to obtain well sampled radial profiles of the objects and measure their deviation from that of a stellar source. This procedure efficiently helps to overcome the problems caused by the WFC2 undersampling. Furthermore, to identify areas of multicolor space where quasars might be expected, we generated synthetic quasar spectra in the range $1.0 < z < 5.5$ including effects of intrinsic emission lines and absorption by Ly α forest and Lyman-limit systems, and computed expected quasar colors. We also developed routines to determine the completeness of our data to point sources in the observed filters. The data are 90% complete at 26.2^m, 28.0^m, 27.8^m, 26.8^m in the F300W, F450W, F606W and F814W filters respectively. We find 41 compact objects in the HDF: 1 pointlike object with colors consistent with quasars but

¹Based on observations with the NASA/ESA Hubble Space Telescope obtained at the Space Telescope Science Institute, which is operated by Association of Universities for Research in Astronomy, Incorporated, under NASA contract NAS5-26555.

²Currently at the NAPL, Keble Road, Oxford (UK), OX1 3RH

inconsistent with that of ordinary stars, 7 pointlike objects with colors consistent with quasars or stars; 18 stars; and 15 slightly resolved objects, 12 of which have colors consistent with quasars or stars. The latter objects could be resolved active galactic nuclei or regions of intense star formation. We estimate the upper limit of unresolved and slightly resolved quasars/AGNs with $V_{606} < 27.0$ and $z < 3.5$ to be 20 objects (16,200 per deg^2). We independently recovered a resolved, star-forming galaxy with a spectroscopically confirmed redshift of 3.368 and 5 spectroscopically confirmed stars. Both provide confirmation for the validity of our color and morphological modeling.

We make a detailed comparison with previous studies of the HDF. We find good agreement among different authors on the number of stars in the HDF and the lack of quasar candidates with $z > 3.5$. We find more quasar candidates than previous work because of our more extensive modeling and use of the color information. Spectroscopic observations of the candidates are needed to determine which, if any, are quasars or AGNS.

Subject headings: galaxies: compact — quasars: general — surveys

1. Introduction

The study of the high redshift universe has seen a dramatic development over the last two years with the discovery of a large population of star-forming galaxies at redshifts $z \sim 2 - 4$ (Abraham et al. 1996; Ellis 1997; Clemens & Couch 1996; Maoz 1997; Elson, Santiago & Gilmore 1996; Zepf, Moustakas & Davis 1997; Steidel et al. 1996; Lowenthal et al. 1996; Mobasher et al. 1996; Lanzetta, Yahil & Fernandez-soto 1997; Phillips et al. 1997; Madau et al. 1996; Guzman et al. 1997; Pettini et al. 1997). The Hubble Deep Field (HDF, Williams et al. 1996) has played a key role in this development, since it provides not only the deepest images for multi-color selection of “Lyman break” galaxies but also morphological and size information for high redshift galaxies (Bouwens, Broadhurst & Silk 1997; Berlind & Conti 1998). As we go to fainter and fainter magnitudes, morphological information for individual objects becomes harder to extract (Abraham et al. 1996) and the best approach to understand these objects is through a multi-dimensional analysis of the populations of objects as a whole. From this perspective, objects detected in the HDF can be regarded as the components of a multi-dimensional parameter space, whose axes include at a minimum the apparent magnitude, three colors, and an angular size. Larger and brighter galaxies are also interesting in their own right because the morphologies of these relatively high-redshift objects can be compared in detail to those of present day galaxies; these sorts of studies are being carried out by other authors, such as the members of the Medium Deep Survey team (Roche et al. 1996; Mutz et al. 1994).

Acquired during ~ 150 orbits near the north galactic pole in December 1995 and imaged in four filters: F300W (U_{300}), F450W (B_{450}), F606W (V_{606}) and F814W (I_{814}), the data for the HDF resulted from 35 hours of exposure time in B_{450} , V_{606} and I_{814} and 45 in U_{300} . The unique feature of the HDF images is their ability to resolve extremely faint extended sources and to distinguish them from point sources down to an unprecedented magnitude (see Section 3). Several authors have also used this features to put constraints on the nature of the dark matter (Flynn, Gould and Bahcall 1996 hereinafter FGB; Colley et al. 1997; Kawaler 1996) and on galaxy and structure formation in the universe (Metcalf et al. 1996; Baugh, Cole & Frenk 1996; Colley et al. 1996; Sawicki, Lin & Yee 1997; Van der Bergh et al. 1996). It is natural to make use of this intrinsic property to look for faint quasars in the HDF.

Quasars are believed to be the visible manifestation of the accretion of matter onto supermassive black holes and, being among the most distant and luminous objects in the universe, hold a primary role as cosmological probes. Due to their stellar-like nature, quasars cannot be distinguished from stars in single images of the sky, as galaxies can. However, multi-color selection techniques have proven very successful in recent years in selecting quasar candidates at high redshifts (Warren et al. 1994; Kennefick et al. 1995; Hall et al. 1996 and references therein). At lower redshifts ($z < 2.2$), quasars can be selected in the U_{300} and B_{450} images by adopting the standard UV-excess technique. As Ly α moves into the V_{606} filter, quasars at $z > 3.5$ can be selected on the basis of the $B_{450}-V_{606}$ color, and as Ly α moves into the I_{814} filter and continuum absorption by Ly α becomes stronger, the $V_{606}-I_{814}$ color will serve as a powerful selector of quasars

at $z > 4.8$. In addition, by making use of the excellent angular resolution of HST, we can add a morphological selection criterion to our color selection criteria. This will enable us to select those objects whose morphological *and* color characteristics are consistent with them being quasars or active galactic nuclei (AGN).

The main purpose of this paper is to find spatially unresolved quasar candidates which have colors consistent with quasars in the range $1 < z < 5.5$. Section 2 explains the trade-offs involved in the choice of the lower resolution crude combine images as opposed to the higher resolution drizzled images. As observed below, we chose to use the lower resolution crude combine images for object detection together with the raw dither positions for PSF modeling because they improved results on scales smaller than 1 pixel.

Section 3 describes the steps involved in computing the detection completeness of the HDF to point sources. We did not simulate artificial fields with HDF-like properties, instead we used the original crude combine images and carefully added artificial point sources in a wide range of magnitudes. A model PSF was created for each chip and filter from a subsample of the stars found in the HDF by FGB. The number of detected point sources as a function of magnitude provides stringent limits on our detection efficiency at faint magnitudes and will be used to constrain object classification.

Direct object classification from the crude combine images is not possible due to the undersampling of the WFPC2. In Section 4 we describe the steps used to overcome this problem and obtain spatial information on objects within a 1 pixel radius from their center. This allowed us to produce a list of objects with characteristics typical of stellar-like sources. In Section 5, by generating synthetic quasar spectra in the redshift range $1 < z < 5.5$ and convolving them with the HDF filter curves, we determine what colors to expect for quasar candidates. Then we combine the spatial and color information to produce a list of candidate quasars in Section 6. In Section 7 we present an estimate of the upper limit of quasar candidates and discuss the results. We compare our results with previous work in Section 8 and consider future searches for AGNs in Section 9.

2. Image Selection and Source Detection

In order to reduce the photometric errors due to flatfielding uncertainties, the HDF team made the decision, early in the planning stage, to carry out the HDF observations at roughly 9 different pointing positions per filter, spanning a range of $2.6''$. This procedure called “dithering” has the secondary purpose of trying to recover some of the information lost due to the undersampling of the WFPC2 detectors. This is achieved by allowing sources to be sampled in different portions of a pixel at each dither position.

The HDF data were reduced two times. Version 1 accounts for processing up to January 1996. Version 2 was released February 1996 and contains a new set of images obtained with

a new technique for the linear combination of images known formally as variable-pixel linear reconstruction and informally as “drizzling” (Fruchter & Hook 1996). The drizzled images produced have a new pixel scale 2.5 times smaller than the original $0.1''$ typical of the WFPC2. While higher resolution is an attractive feature, the interpolation scheme used alters the radial profiles of the sources in the images and introduces correlated noise among neighboring pixels. These effects result in a widening of the PSF from as little as 5% for Poisson noise free images, to as much as 15% for real HDF images. Correlated noise results in an underestimated pixel-to-pixel rms noise by a factor of 1.9 (Williams et al. 1996).

We thus decided to use the Version 1 crude combine images for object detection and photometry. These are images at different dither positions shifted (with integer pixel shifts) and combined with a median filter to produce a median image at the original pixel scale with no correction for geometric distortion, but with a minimal amount of interpolation. Even though individual images show curvature of a few percent in the background within 200 pixels of the edge of the chip, these variations are reduced to less than 1% when multiple frames are stacked together (Williams et al. 1996).

The use of the median in the image combination may lead to systematic errors in the photometry if the images are not perfectly registered. The HDF team checked the registration of the individual images by comparing the positions of several bright sources. They found that the images at each dither position were registered well within the errors of such a comparison. Two unexpectedly large ($0.8''$) shifts have been treated as separate dither positions (Williams et al. 1996). We are therefore confident that accurate photometry can be performed on the crude combine images. However, to reliably distinguish stars from galaxies at faint magnitudes, we need to be able to sample the radial profile within the inner central pixel (FGB). To achieve this accuracy, we revert to the use of the raw dither images in all four filters. Section 4 will describe why such a combined approach is crucial to a reliable object classification.

We used the FOCAS analysis package (Jarvis & Tyson 1979; Valdes 1982) for object detection run under the SKICAT catalog management software (Weir et al. 1995) to detect objects in the HDF crude combine images. To prepare the frames for object detection, we trimmed them of bias regions and registered them to the nearest pixel in all four filters. To optimize our detection algorithm we tested a range of convolution kernels (a series of Gaussian kernels and the FOCAS built-in one) for data smoothing in order to find the one most suitable for the objects in the HDF. In general, spurious detections are introduced by either a poor noise estimate around the object or by object sizes that are not well matched by the detection kernel. The Gaussian filters ranged in FWHM from that of the point-spread-function of the HDF (~ 1.2 pixels) to 10 times this width. The Gaussian filter with twice the FWHM of the HDF outperformed the other Gaussian filters. The FOCAS built-in filter, however, performed the best overall by maximizing the number of detected objects while minimizing spurious detections.

Consequently, we ran FOCAS on all images and, after the value of each pixel was convolved

with the FOCAS built-in detection kernel, we required each detected object to have a minimum of 6 contiguous pixels, or 0.09 square arcseconds, above a detection threshold of 2.5 times the local sky rms. FOCAS then examines these sources for sub-components. This process, however, can break large bright unmistakably recognizable spiral galaxies into many subcomponents which are not independent objects. In order *not* to include these objects in our catalog, we manually merged them back into their parent. A total of 24 objects in 9 galaxies were re-merged.

The newly formed $U_{300}, B_{450}, V_{606}, I_{814}$ catalogs were matched using the pixel coordinates. Aperture photometry was performed for each object in the $U_{300}, B_{450}, V_{606}, I_{814}$ catalogs using the IRAF³ PHOT task with an aperture of 2 WFPC2 pixel radii or $0.2''$. The output from PHOT was then used with the HDF Vega zeropoints and the exposure times in each filter to derive magnitudes for all objects. Photometric errors as a function of magnitude returned by PHOT are shown in Figure 1. Color-color diagrams for $(U_{300} - B_{450})$ vs $(B_{450} - V_{606})$ and $(B_{450} - V_{606})$ vs $(V_{606} - I_{814})$ of all the objects in the HDF with a 5σ detection in the 4 filters are shown in Figures 2 and 3 respectively. The figures show clearly that most of the objects have $-0.2 < (B_{450} - V_{606}) < 1.4$ and $0 < (V_{606} - I_{814}) < 1.5$. The lack of a very red compact population is evident and not entirely new. Current findings from medium-deep surveys emphasize the presence of the rising fraction of faint systems with irregular morphologies suggestive of rapid stellar evolutionary processes (Glazebrook et al. 1995; Driver et al. 1995).

3. Completeness

A fundamental step to achieve a useful catalog of the objects in the HDF is to understand how often stellar objects failed to be detected as a function of magnitude in each filter and in each separate WFPC2 chip, i.e. the completeness limits of the dataset to point sources. To determine the completeness of the HDF, we adopted the straightforward approach of adding artificial point sources to the HDF frames using the IRAF/ARTDATA task over a wide range of magnitudes. Adding artificial point sources to the actual HDF frames does not require the generation of artificial images that mimic the observed properties of the HDF and has the further advantage of matching the noise properties of the data.

In performing any completeness test, particular attention must be paid to the PSF of the added sources. This should resemble as closely as possible that of the actual data, including its noise properties. We decided to construct a PSF template using the sample of stars found in the HDF by FGB. We selected unsaturated stars brighter than $V_{606} \sim 25$ in each chip. We compared each candidate star radial profile with a PSF generated by TinyTim (Krist 1993), a sophisticated PSF simulation software that takes into account chip and optics distortions to

³IRAF is distributed by the National Optical Astronomy Observatories, which are operated by the Association of Universities for Research in Astronomy, Inc., under cooperative agreement with the National Science Foundation.

generate a model PSF. To further improve our PSF templates, we derived radial profiles from a sample of stars extracted from the Hubble Space Telescope PSF Library. The agreement among these three model PSFs was excellent. However PSF variations among different chips prompted us to generate PSF templates for each of the 3 chips in each filter rather than to produce a global HDF PSF. This approach, while adding a further layer of complexity to the analysis, will turn out to be particularly useful during the morphological classification phase. A template PSF used in the completeness test for Chip 4 in the I_{814} filter is shown in Figure 4. The figure shows the distance in pixels from the center of the template against the fraction of light falling on that pixel. The flux has been normalized to the total flux within a 4 pixel radius aperture. The WFPC2 undersampling is evident.

It should be noted that TinyTim implicitly assumes that the source is always centered on the central pixel. This is clearly visible in Figure 4 where all the filled circles, representing the TinyTim model, are exactly positioned at fixed distances from the central pixel. This artifact is solely introduced by the modeling of TinyTim. Real sources will be randomly positioned with respect to the central pixel and hence produce a PSF that samples a wider range of distances from the center. We will in fact show in Section 4 how the actual position of the source can be used to produce a well sampled PSF well within the innermost central pixel, thereby allowing an accurate morphological separation between stars and galaxies.

To measure the completeness of the HDF to point sources, we added 10 template stars to each chip in each filter ten times for a total of 100 stars per magnitude bin. We then applied the same detection procedure adopted for the original HDF frames, using FOCAS, and recorded the number of added point sources that we recovered as a function of magnitude. In the range of input magnitudes $23 < m < 32$ we observed a slow linear decline before the sharp cutoff at the detection threshold. This change in behavior occurs at the $\sim 90\%$ completeness level. In Figure 5 we show the percentage of added template point sources that were recovered as a function of magnitude in each chip. Error bars represent a 1σ uncertainty around the mean value.

As clearly shown in Figure 5, there are small differences among the filters in different chips. At the 90% completeness threshold the B_{450} and V_{606} data have, within the errors, the same behavior and reach depths that differ on average by only 0.1 magnitudes. However, while at 90% completeness the B_{450} image is deeper than the V_{606} image, there is an inversion at the 50% level where the V_{606} image becomes deeper. In Table 1 we list the 50% and 90% completeness for all chips in each image.

4. Compact Source Selection

Bahcall et al. (1994) have shown how radial profiles can be effectively used to separate stars from galaxies. However, to distinguish stellar from extended profiles we need at least 5 times more photons than required for a simple detection (FGB). We will therefore restrict our classification to

all the objects with a 5σ detection in B_{450} , V_{606} and I_{814} (U_{300} being optional), and ~ 1 magnitude brighter than the 90% completeness limits for each filter. The resulting total number of objects detected in (U_{300}) B_{450} V_{606} I_{814} is 1709. Hence our search for point-like sources will not include objects fainter than $U_{300} \sim 25.2^m$, $B_{450} \sim 27.0^m$, $V_{606} \sim 27.0^m$, $I_{814} \sim 26.0^m$.

The steps undertaken to produce a reliable classification are described in detail below and are summarized as follows:

1. the objects in the crude combine images were shifted according to all the available dither positions in each filter (from a minimum of 8 to a maximum of 11);
2. all objects were identified separately in each dither and their radial profiles computed;
3. all dither profiles were then combined together to produce a densely sampled profile of each object on sub-pixel scales;
4. each profile was then compared to that of the PSF and its departure from the PSF measured;
5. simulations were used to predict the expected departure as a function of magnitude.

A fundamental step in constructing the radial profiles is determining the location of the center of the object to better than 0.1 pixels by making use of the symmetry of the object about its center. To overcome the poor PSF sampling of the WFPC2, we used a technique that combines the raw dither frames to obtain a well sampled radial profile in each filter of all our objects. This task is accomplished by producing a shifted catalog of objects (using the image shifts made available by the HDF team) for each dither position, leaving the single images untouched and therefore avoiding any flux interpolation among aligned frames. Each catalog is then used as an input to the IRAF/RADPROF task that computes the radial profiles and accurately re-centers them. We used 9, 8, 11 and 8 separate dither positions in U_{300} , B_{450} , V_{606} and I_{814} respectively. The different number of dithers used reflects the exclusion of frames affected by the characteristic X-pattern due to scattered light from the Earth (Williams et al. 1996). For each object, the single dither profiles obtained are then combined together to produce a well sampled radial profile that will in turn be used for classification (Figure 6).

The few unsaturated stars were used to construct PSF templates upon which to base classification. Each PSF template was in turn compared with radial profiles from a large number of stars that appear in the WFPC2 exposures at low galactic latitude. Again, the agreement was excellent. The advantage of using single dither profiles to overcome the WFPC2 undersampling is evident in Figure 6 when compared to the crude combine profile in Figure 4. Since the radial profile is sampled in many adjacent pixels at different distances from the image center, adding dithers together produces a densely sampled profile well within the innermost pixel. Figure 6 shows the radial profile of a 21.2^m magnitude star. Each filled circle represents a pixel in one of the 11 dithers used in constructing the profile. The flux has been normalized to the total flux within 4 pixels.

To better model the PSF, we fit a Moffat profile (Moffat 1969) to the few unsaturated stars in each chip and in each filter of the following form:

$$I(r) = I_0 \left(1 + \left(\frac{r}{\alpha} \right)^2 \right)^{-\beta} \quad (1)$$

where I_0 is the central intensity and α is a measure of the width of the profile and can be easily related to its FWHM. The choice of a Moffat profile as opposed to, for example, a Gaussian, was motivated by the parameter β , which allows for a better modeling of the data in the wings of the distribution where most of the points reside. To further constrain our fit, we also paid much care to the way the weights were assigned to the single points. We decided to weight more “signal” rather than “noise” by assigning larger weights in the fit to the innermost points (those within 0.6 pixels of the center). After normalizing the profile to the total flux within the innermost 4 pixels, we chose weights that are proportional to the Poisson noise at each point of the profile. For stellar sources like the one in Figure 6, the normalized profile contains more than 90% of the total light within the innermost 1.4 pixels. Furthermore, by assigning small weights to points at large distances from the center of the object, we force our fitting algorithm to focus on the amount (I_0) and concentration (α) of the signal rather than allowing it to find low χ^2 solutions driven by the concentration of points at distances greater than 2 pixels. During classification, as we will later show, this approach will essentially reduce the available degrees of freedom in our fit from 3 to 2, thereby simplifying our further analysis.

Once all the Moffat parameters were found and the 12 PSF templates created (one for each chip in each filter), we fit a Moffat profile to all the remaining objects in our catalog, setting the value of the parameter β to that of the appropriate (chip and filter) PSF. The parameter β controls the “rate of decay” of the tail of the Moffat distribution. By fixing β to its appropriate value, we constrain our fitting algorithm to minimize χ^2 for a given tail dependency. This procedure returns I_0 and α (or the FWHM of the profile), which are now directly comparable to those of the template PSFs. Among these parameters, I_0 is not only the most stable and physically meaningful but, most importantly, is the most sensitive for discriminating between stars and extended objects. Figure 7 shows one such fit for a galaxy. For comparison, the PSF template is also shown. It is clear that I_0 is indeed a well suited parameter for star/galaxy separation. Candidate selection, however, requires a further step: the assessment of the scatter in I_0 as a function of magnitude for stellar objects.

For the selection of the stellar candidates, we decided to simulate stars of different magnitudes and compute their Moffat parameters as was done for real HDF objects. In this particular case, however, we need to simulate a “dither star” of a given magnitude (i.e. a single star viewed at separate dither positions) and then combine its dither radial profiles to form a densely sampled profile in exactly the same way as was done for the real data. This approach is again quite robust since the artificial stars added to the single dithers match perfectly the noise properties of that particular dither, filter and chip.

Template stars were created using the IRAF/ARTDATA task where the PSF parameters for a Moffat profile were taken from the relevant chip and filter. We added 10 stars per magnitude bin in the range $23 < m < 29$, computed their radial profiles, fitted a Moffat profile and recovered I_0 and α . Figure 8 shows the typical behavior with magnitude of the central intensity parameter I_0 for all objects in the V_{606} filter. The dashed lines represents the 95% confidence interval (given by our simulations) within which stellar candidates lie. As the template star magnitude approaches the completeness limit of the data, the errors increase past the point of reliable classification. This limit, in magnitude, is roughly $\sim 0.75^m$ brighter than the 90% completeness limit in each filter, with the exception of the U_{300} filter where the limit is $\sim 1^m$ brighter than the 90% completeness limit due to the low quantum efficiency of the U_{300} detector which is virtually noise limited, as opposed to the other filters which are nearly sky-noise limited (Williams et al. 1996).

Using the central intensity parameter I_0 and its variation as a function of magnitude, we can now select compact objects in each filter. We find 57, 36, 32 and 15 objects in U_{300} , B_{450} , V_{606} , I_{814} respectively. However, not all of these objects have detections in all 4 filters (mainly because of missing U_{300} detections). For candidate selection we will require a candidate to be selected as compact in at least one of the 4 filters. The number of independent objects meeting this criterion is 41. These objects are listed in Table 2 along with their magnitudes and coordinates both on the sky and on the drizzled images.

For classification purposes we will select objects classified as compact in at least one of the three redder filters: B_{450} or V_{606} in the $(U_{300} - B_{450})/(B_{450} - V_{606})$ plane and V_{606} or I_{814} in the $(B_{450} - V_{606})/(V_{606} - I_{814})$ plane respectively. All 41 objects in Table 2 meet this requirements. This first stage of our analysis efficiently extracts all the compact sources in the dataset down to the 90% completeness limit. One confirmation of the effectiveness of our selection algorithm is that we recover all 17 stellar-like objects found by eye by FGB (see Table 5). While most of these objects are relatively bright sources whose profiles are unmistakably classified as stars (both by an eye search by FGB and our algorithm), as we approach the completeness limit of the dataset, galaxy contamination becomes important and a clear classification is not possible on morphological grounds only (see Figure 8). Color information becomes therefore an essential tool to help us distinguish among compact galaxies, stars and quasars.

Before proceeding in our analysis, however, we realized that our morphological parameter space allows for an additional assessment of the “degree of compactness” of each object independent of color. In fact, the quantity I_0 does not in itself provide for a measure of the deviation of a given object’s profile from that of the PSF but acts more like a minimum threshold as a function of magnitude for selecting compact objects. While it may seem that combining I_0 with the FWHM or α would be a better choice to assess this deviation, our tests on simulated stars show that a more stable measure of such a deviation as a function of magnitude is obtained by taking the ratio of the peak to total flux within 4 pixels and comparing it to that of known stars in the HDF. This new parameter can be formally defined as:

$$\Delta = 1 - R_{obj}/R_{psf} \tag{2}$$

where $R_{obj} = I_0/I_{tot}$ is the ratio of the peak to total flux for each of our 41 objects and R_{psf} that of the PSF. The parameter Δ was used for classification only in the three redder filters because higher noise in the U_{300} images made them not useful for this purpose. As done for I_0 , we computed Δ for our simulated stars and obtained the range of variation of Δ as a function of magnitude and filter. With this new quantity in hand, we can now separate stellar from compact objects in a more objective fashion and hence try to reduce galaxy contamination for those objects close to the limiting magnitudes for classification. We will require objects to be within the 3σ confidence intervals of the PSF in at least 2 of the 3 redder filters in order for them to be classified as quasars. Our confidence intervals as a function of magnitude are tabulated in Table 3.

As an immediate application, we measured Δ for all 17 objects found by FGB (see Table 5). As mentioned before, most of these objects are quite bright and are easily classified as stars based on the appearance of their radial profiles, the value of their I_0 parameter and the value of Δ (see Table 2). We then decided to re-examine only the 6 faintest objects in the FGB sample (all of which have $V_{606} > 26.5$) in order to assess whether any of them had been erroneously classified as stars. These 6 objects, together with the additional 24 that we classified as compact, constitute our final sample. This sample of objects will be analyzed in detail in the following section, where we will use color information for the objects along with simulated quasar and stellar colors to divide all the objects in the sample into three groups: stars, quasars and compact galaxies. The latter refers to those objects that do indeed appear compact, according their I_0 value, but either have a significant deviation from the stellar profile (indication of the presence of an extended component) or do not exhibit colors consistent with stars or quasars.

5. Color Selection

Having morphologically selected compact source candidates, we return now to the use of multicolor space to investigate the presence of objects whose colors are consistent with them being quasars. This method has been widely used, with much success, in the past (Newberg & Yanny 1997, Miyaji et al. 1997; Hall et al. 1996; Kenefick et al. 1995; Siemiginowska et al. 1995; Warren et al. 1994; Warren et al. 1991) and its application is quite straightforward. To determine what colors to expect for quasar candidates, we first created synthetic quasar spectra at redshifts $1 < z < 5.5$ in steps of $\Delta z = 0.1$. In generating these spectra, we assumed a power law continuum of the form $f_\nu \propto \nu^\alpha$ and Gaussian profile emission lines of FWHM=5000 km s⁻¹. Rest frame equivalent widths were taken from Wilkes et al. (1986) for Ly α , N V, Si IV, C IV, and C III, and from Warren et al. (1991) for O VI.

Wilkes et al. (1986) give the rest frame equivalent widths (EW) of Ly α of a typical quasar as 65Å. We have considered three line strength cases by varying the strength of the Ly α line, but keeping the EW ratios fixed: EW(Ly α) = 32.5, 65.0, and 130.0. This range of EW includes 90% of the objects in the Wilkes et al. sample (95% if we include two more objects that fall outside the range by only 1Å). We have also allowed for a variation in the continuum slope by

creating spectra with $\alpha = -0.50, -0.75, \text{ and } -1.00$ for each line strength and redshift. Another important factor in computing the expected colors of quasars is the continuum drop blueward of $\text{Ly}\alpha$ due to intervening absorption. We have used models of the absorption due to the $\text{Ly}\alpha$ forest, Lyman-limit systems and Lyman continuum absorption as a function of redshift. For full details, see Kennefick et al. (1995) and references therein. For each redshift, line strength, and continuum slope considered, we generated five different quasar spectra with different realizations of the absorbing systems for a total of 1845 synthetic spectra.

We convolved the synthetic spectra with the HDF filter curves to obtain simulated quasar colors. Photometric magnitude errors were added to the simulated colors according to the distribution shown in Figure 1; we assumed a Gaussian distribution of errors at a given magnitude down to $V_{606} = 29.4$, corresponding to a $\sim 3\sigma$ detection. We show in Figures 9 and 10 the loci that contain 99% of the simulated quasars. We will use these loci to define the regions in color-color space for quasar candidates. We consider this to be the most suitable approach due to the lack of a quasar database in the four WFPC2 filters used for the HDF. Kennefick et al. (1997) have shown for the DMS ground based survey that an identical modeling approach is in good agreement with the observed quasar colors.

The colors of the morphologically selected compact sources in the HDF can now be directly compared to those of model quasars in Figures 9 and 10. The observed points are denoted by circles. For objects not detected in U_{300} , we adopted a 3σ limiting magnitude value of 26.9, according to the results shown in Fig. 1. This limit is based on photometric measurements and error estimates of all the detected objects in the HDF. In this case, the limit corresponds to a flux value 3σ above zero.

It is worth mentioning that since we did not require objects to be detected in U_{300} , the presence or lack of a U_{300} detection does not limit our subsequent color analysis or the limiting magnitude we give below in §7. In fact, Figure 9 shows that there are no objects with color upper limits that would overlap our quasar locus for low redshift objects. As for the $(B_{450} - V_{606})/(V_{606} - I_{814})$ color-color plane, the U_{300} information was not used to select high- z candidates. We also compare the colors of our objects to those of typical stars. The stellar points were derived from the Bruzual-Persson-Gunn-Stryker (BPGS) spectrophotometric atlas available through the STSDAS/SYNPHOT package under IRAF. This atlas is an extension of the Gunn-Stryker optical atlas into both the UV and the infrared (Gunn & Stryker 1993). The IR data are from Strecker et al. (1979) and the IR and optical data were tied together by the $V - K$ colors. The transformation from standard Johnson/Cousin passband colors to HST colors was obtained using SYNPHOT by convolving the spectrum of each of the stars in the BPGS spectrophotometric atlas with the HST filter and chip response curves.

6. Candidate Selection

Now we are able to use the index of compactness, Δ , and the color information in Table 2 to classify each object as a quasar candidate, star, or compact galaxy⁴. We will consider objects with $\Delta < 3\sigma$ as starlike and those with $\Delta > 3\sigma$ as compact galaxies. We use the color information to place the objects in one of three categories: 1) colors on or within the quasar locus and away from the stellar locus; 2) colors consistent with either quasar or stars; or 3) colors not consistent with quasars. Objects in categories 1 and 2 are divided according to whether their colors are consistent with low-redshift quasars (lz - ultraviolet bright, see Figure 9) or high-redshift quasars (hz - see Figure 10). Objects in category 3 are classified as stars or galaxies according to their Δ parameter.

The results of this classification process are given in Tables 4, 5, and 6. Table 4 contains the pointlike objects in the HDF that are in color categories 1 and 2. There is only one candidate in category 1, ID0094, and it is a lz object. The remaining entries in Table 4 are all in category 2.

Table 5 lists all the pointlike objects in the HDF that we classify as stars on the basis of having $\Delta < 3\sigma$ and colors in category 3. The list contains 16 of the 17 FGB stars and two additional objects that meet our criteria. We place the 17th FGB star in Table 4 because it is in our color category 2. As a further confirmation of the validity of our approach, 5 of our candidate stars (0276, 0341, 1429, 1610 and 3121) have been spectroscopically confirmed by Cohen et al. (1996) to be indeed stars.

Table 6 lists the 15 compact objects with $\Delta > 3\sigma$, which we consider to be slightly resolved galaxies. Of these, 10 are in color category 1, 2 in color category 2, and 3 in color category 3. We will consider the objects in the first two categories as potential AGN candidates in which the host galaxy is being detected, although we recognize that colors alone cannot distinguish them from compact galaxies undergoing intense star formation. In fact, during the early development of our procedure, we identified a compact object with the colors of a $z \sim 3.5$ quasar. The object did not remain in our list of candidates because it was spatially resolved by the procedures we finally adopted for the selection of compact objects. However, we do note that Lowenthal et al. (1996) found it to be an (narrow) emission-line galaxy with $z = 3.368$ (our ID0627 = their hdf2_0705_1366). The object is shown as a filled square in Figure 10. It serves as both a confirmation of our modeling techniques and an illustration of the problem of color degeneracy between quasars/AGNs and starbursts.

7. Discussion

⁴A detailed description of the color and morphological properties of the compact sources in the HDF is available from the first author.

7.1. Estimate of the Upper Limit on Quasar Candidates in the HDF

First, we note that there are no candidates with colors indicating that they have $z > 3.5$; all the candidates in Tables 4 and 6 are expected to have $z < 3.5$. We use the following procedure to estimate the upper limit of such quasars and AGNs in the HDF:

1. There is 1 unresolved object with quasar colors, ID0094.
2. There are 7 unresolved objects whose colors are consistent with either stars or quasars (the remaining objects in Table 4).
3. There are 10 slightly resolved objects in Table 6 with quasar colors. We include them because of the possibility that they are quasars in which the host galaxy is being detected.
4. There are 2 slightly resolved objects in Table 6 whose colors are consistent either with stars or quasars. We include them for the same reason as given above.

The sum of the objects listed above is 20, which we take to be our estimate of the upper limit of quasar and AGN candidates in the HDF for $V_{606} \leq 27.0$ and $z < 3.5$. We surveyed 4.44 arcmin² of the HDF⁵ so the upper limit in surface density is 16,200 per deg². Of course, spectroscopic observations of the candidates are needed to determine which objects if any are quasars or AGNs.

How does this upper limit compare with expected values? Because the HDF reaches fainter than any well-studied quasar survey with spectroscopic confirmation of many objects, one approach is to extrapolate the results of quantitative surveys done to brighter limiting magnitudes. For example, the results of Boyle et al. (1988, BSP) and Warren et al. (1994, WHO) cover the redshift range $0.1 < z < 4.5$ down to observed magnitudes of about 20⁶. We find that the BSP luminosity function, which is for $z < 2.2$, predicts 824 quasars per deg² with $B \leq 27$, or 1 quasar in the area of the HDF that we surveyed, consistent with our upper limit. For higher redshift objects, $3.0 < z < 4.5$, the WHO luminosity function predicts 2570 quasars per deg² with $R \leq 27$, or 3 quasars in the HDF, also consistent with our upper limit. Another approach is to use the Hartwick-Schade (1990) compilation of cumulative surface densities of quasars. A linear extrapolation of the log N(<B) vs. B data in their Table 3b for $B \geq 19.0$ leads to 8,200 quasars deg⁻² for $0 < z < 2.2$ and 12,000 quasars deg⁻² for $0 < z < 3.3$. These values still within our upper limit although they are significantly larger than the BSP extrapolation, for example. However, the BSP luminosity function has a two-power law form that evolves with redshift. It is

⁵A 35 pixel border was excluded for each chip to avoid edge distortions and an incorrect estimate of the sky background for objects too close to the edge of the chip.

⁶The Schmidt et al. (1995, SSG) survey has more quasars than the WHO survey but is not suitable for this comparison. The SSG luminosity function is only valid for the interval $-27.5 < M_B < -25.5$, where the slope is steeper than for the less luminous quasars that HDF can reach.

not surprising that its extrapolation well beyond the limits of the data on which it is based differs from the simple extrapolation of the Hartwick-Schade number count data.

The important next step will be to confirm the number of actual quasars and AGNs in the HDF (for example, with spectroscopic observations) so that we can pin down the faint end of their luminosity function at high redshifts. This is also crucial to estimating the degree of ionization of the intergalactic medium that quasars contribute at high redshift (Miralda-Escudè 1998). Similarly, establishing the number of faint quasars with $z < 3.5$ is important to understanding the early formation of quasars and the structures in which they reside. Haiman et al. (1998) note that the lack of $z > 3.5$ candidates in the HDF already is constraining models of structure formation.

7.2. Faint Blue Galaxies in the HDF

We concur with other studies of the HDF, e.g., Elson et al. (1996, ESG), that one of its striking features is the presence of a significant number of faint, blue, compact galaxies, many of which are at high redshift and are regions of intense star formation. It is likely that many of the objects in our Table 6 are in this category. As noted by ESG, many have nearby companions or show evidence for having an extended component. Some are among the bluest objects in the HDF (Figure 9). Others are blue in $U_{300} - B_{450}$ but redder in $B_{450} - V_{606}$ than our model quasars, which is an indication that they may be compact, narrow, emission-line galaxies.

7.3. White Dwarfs in the HDF?

If white dwarfs in the halo of the Milky Way constitute up to 50% of the dark matter, as suggested by early MACHO results (Alcock et al. 1997), then white dwarfs should be observable in the HDF. We investigated this possibility with the following procedure: 1) white dwarf candidates should be unresolved, $\Delta < 3\sigma$; 2) they should fall in areas of the $(U_{300} - B_{450})/(B_{450} - V_{606})$ diagram where white dwarfs would be expected, and 3) any such objects should also have $(B_{450} - V_{606})$ and $(V_{606} - I_{814})$ colors consistent with white dwarf colors. We found that objects ID0094, ID0134, ID0212, and ID1515 meet criteria 1 and 2 but not 3 (they are too red). Thus, we find no good candidates for white dwarfs in the HDF. This is either a warning flag for the MACHO results or a signal that the fraction of white dwarfs brighter than the detectability limit of the HDF is much smaller than predicted by current halo white dwarf formation and evolution models (FGB; Kawaler 1996). In addition, all the pointlike sources we identify are quite blue and faint and thus appear too blue to be white dwarfs older than a few Gyrs and therefore cannot be a significant fraction of the Milky Way halo.

8. Comparison with Other Searches of the HDF

Here we compare our results with those of other groups who have searched the HDF: Williams et al. (1996), FGB, ESG, and Mendez et al. (1996, MMMBC). We begin with the Williams et al. article, which provides the description of the HDF project, the data reduction procedures, and the catalog of the 3500 objects they found. Their catalog gives positions and the main photometric parameters of the objects and is a fundamental reference for the HDF. Williams et al. used FOCAS, as we did, to produce their catalog. They did not attempt a detailed analysis of the objects nor a separation of stars and galaxies. We found in comparing our list of compact objects in Table 2 that each object was in the Williams et al. catalog and that the agreement of the X,Y positions was excellent.

Turning to the FGB work, we have already noted that we recovered all 17 stars they found. FGB used the individual dither images to construct radial profiles for objects and then merged them to obtain dense sampling, as we have done. The main difference is that FGB selected stars by visual inspection of the profiles, while we used the procedures described in this article. We found 2 stars in addition to the 17 FGB stars, and 7 more quasar candidates. This is probably due to our use of the Δ parameter and all 4 of the photometric bands in the HDF data.

Next we compare our results with ESG, who used DAOPHOT to find and make photometric measures of objects in the HDF. They list 9 candidate low-mass stars (their Table 1) and 50 faint, blue, unresolved objects (their Table 2). All 9 star candidates in their Table 1 are in our list of stars, Table 5⁷. We find in addition 5 objects we consider to be stars, ID0134, ID0273, ID0341, ID1610, and ID3121. The 15th, a star in our list, ID0276, is object 2-14 in their Table 2. Of the 8 quasar candidates in our Table 4, 2 are in their Table 2: ID0563 = their object 2-7 and ID1515 = 3-4. ESG believed there were no quasar candidates in the HDF, but their results were based only on measures of the V_{606} and I_{814} images. We agree with them that there are no high-redshift, $z > 3.5$, candidates in the HDF. However, as discussed above, we do find low-redshift candidates from consideration of the $(U_{300} - B_{450})/(B_{450} - V_{606})$ diagram.

Turning to the 50 faint, blue, unresolved objects of ESG, we find that only 6 of them are in our list of compact objects in Table 2. There are only 3 other objects in their Table 2 that are brighter than our classification limit⁸. According to ESG, all 3 are either members of a group or a chain and thus likely to be parts of galaxies, in accordance with our classification. The other 41 are fainter than our classification limit. ESG note that about half of their faint, blue objects have companions within 1 arcsec and think the objects likely are compact regions of intense star

⁷Note that the X,Y coordinates of both ESG and MMMBC differ from those of our system and the Williams et al. system. The offsets are $\Delta X, Y(ESG - Williams) \approx 76, 76$.

⁸Note that our magnitude differs from ESG in the sense that $V_{606}(Conti et al.) - V_{606}(ESG) \approx 0.4$ as determined from the stars measured in common. The difference arises from the different apertures and different photometric routines that were used.

formation.

Finally, we compare our results with those of MMMBC, who used SEXTRACTOR on the combined V_{606} and I_{814} drizzled images to search for stars in the HDF. They found 14 point-like objects, of which they believe 8 are stars and 6 are most likely unresolved extragalactic objects because of their color. We note that the 10 brightest objects in their list are all in our list of stars, Table 5. The 4 remaining objects are all fainter than our classification limit. They considered that there were no quasar candidates in their lists, but their approach was quite different from ours. They did not make use of the $(U_{300} - B_{450}) / (B_{450} - V_{606})$ color-color plane. Furthermore, it is not clear to us how their use of V_{606} vs $(B_{450} - V_{606})$ and I_{814} vs $(V_{606} - I_{814})$ diagrams constrains the existence of quasar candidates. MMMBC claim a 97% completeness at $V_{606} \sim 30$, in considerable disagreement with our determinations, which indicate 50% completeness at $V_{606} = 29.1$.

With regard to the 15 compact objects that we list in Table 6 as galaxies, we note that none of them were selected by ESG, FGB, or MMMBC. Thus there is agreement that these objects are all slightly resolved.

We conclude from our analysis of the HDF data and the above comparison of the 4 different investigations:

1. There is good agreement on the number of stars in the HDF and on the lack of $z > 3.5$ quasar candidates.
2. We find quasar candidates which are expected to have $z < 3.5$, in disagreement with both ESG and MMMBC. We attribute our findings both to the use of all the available color information and to more detailed modeling of quasar colors.
3. Our approach appears to offer better discrimination between unresolved and resolved objects and is better defined quantitatively because of our use of the sub-sampled profiles and our modeling of the detection and classification process.
4. However, our limiting magnitude for classification is brighter than those of ESG and MMMBC because of our use of the individual dithered images for the subsampling.

Thus, the choice of approach depends on the goals of the particular investigation.

9. Future Work: AGNs in the HDF

The present study has concentrated on quasar candidates that are starlike or nearly so in the HDF. This is in accord with the classical definition of quasars as starlike objects of large redshift (Schmidt 1970) and is a logical first step because starlike objects are the most straightforward to detect and analyze quantitatively. However, the classical definition of quasars was developed in the era of 1 arcsec image quality and limiting magnitudes of order 20. The nearly 0.1 arcsec image

quality and 50% completeness magnitude limits fainter than 28 of the HDF quite literally give us a new image of the universe. We may expect two effects to be significant compared to earlier studies: 1) the host galaxy of a quasar can be easier to see, and 2) AGNs of significantly lower luminosity become detectable at relatively high redshift. For example, at $z = 2$, an object with observed magnitude of 27 has an absolute magnitude of -18 ($H_0 = 75$, $q_0 = 0.5$, $f_\nu \propto \nu^{-1}$), five magnitudes fainter than the classical limit for quasars and less luminous than many well-known Seyfert galaxies. Therefore, a search for resolved objects in the HDF with active galactic nuclei is needed.

What will be good ways to find AGNs in the HDF? A first step will be to identify resolved objects whose nuclei have colors consistent with AGNs. However, photometric colors alone will not be sufficient, because intense starbursts at high redshift can produce broad-band colors similar to those of many quasars, as we have already shown in this paper with our recovery of the narrow emission-line galaxy at $z = 3.368$. Spectroscopic observation of broad emission lines and detection of sufficiently powerful X-ray emission are two of the most promising approaches.

Spectroscopic results to date indicate that AGNs appear in only about 2% of faint galaxies in deep surveys with the Keck telescopes. Phillips et al. (1997) found 1 AGN among 54 compact galaxies in the flanking fields of the HDF. Steidel reported at the Young Universe meeting in Monte Porzio in 1997 that 8 of about 350 galaxies with $2.5 < z < 3.5$ and $R \leq 25$ that he and his collaborators had observed were AGNs. Interestingly, the 2% figure in combination with the Madau et al. (1996) results allows us to make another estimate of the number of AGNs in the HDF. Madau et al. (1996) used color selection to identify 69 F300W and 14 F450W dropouts in the HDF. If the 2% fraction of AGNs holds for these objects, the expected number of AGNs in the HDF with $2 < z < 4.5$ is 1.7, comfortably below our estimate of the upper limit. Of course spectroscopic observations are required to establish, for example, what the number of AGNs is at magnitudes fainter than 25, a range that has not yet been explored.

Ultra-deep X-ray surveys with 1-2 arcsec accuracy (or better) positions may offer a superior approach to this question (Hasinger 1998). X-ray emission is a strong signature of activity in galaxies. The combination of a deep survey with AXAF, for example, and deep HST imaging, could provide the most efficient means of identifying faint AGN candidates for follow-up spectroscopy. Whatever approach is used, spectroscopic observations will be essential to determining the relation of quasars and galaxies at high redshift and to understanding the role AGNs play in the formation and evolution of galaxies.

We wish to thank A. Gould, L. Davis, H. Ferguson, A. Fruchter and F. Valdes for useful discussions. We thank the Director of STScI, Robert Williams, and the HDF team for making available such a rich dataset. We acknowledge the anonymous referee for comments and suggestions which helped to improve the overall clarity of the manuscript. Support for this work was provided by NASA through grant number AR-07535.01-96A from the Space Telescope Science Institute, which is operated by Association of Universities for Research in Astronomy, Incorporated, under

NASA contract NAS5-26555. Support was also provided by NSF grant number AST-9519324.

REFERENCES

- Alcock, C. et al. (the MACHO collaboration) 1997, ApJ, 486, 697
- Abraham, R. G., Tanvir, N. R., Santiago, B.X., Ellis, R. S., Glazebrook, K. & Van den Bergh, S. 1996 MNRAS, 279, 47
- Bahcall, J. N., Flynn, C., Gould, A., & Kirhakos, S. 1994, ApJ, 435, 51
- Baugh, C.M., Cole S. & Frenk, C.S. 1996, MNRAS, 282, 27
- Berlind, A. & Conti, A. 1998, in preparation
- Bouwens, R., Broadhurst T., & Silk, J. 1997, ApJ, submitted (astro-ph/9710291)
- Boyle, B.J., Shanks, T. & Peterson, B.A. 1988, MNRAS, 235, 935
- Clemens, D.L. & Couch W.J. 1996, MNRAS, 280, 43
- Cohen, J. G., Cowie, L. L., Hogg, D.W., Songalia, A., Blandford, R., Hu, E.M. & Shopbell, P. 1996, ApJ, 471, 5
- Colley, W.N., Rhoads, J.E., Ostriker, J.P. & Spergel, D.N. 1996, ApJ, 473, 63
- Colley, W. N., Gnedin, O. Y., Ostriker, J. P., & Rhoads, J. E. 1997, ApJ, 488, 579
- Driver, S. P., Windhorst, R. A., Ostrander, J., Keel, W. C., Griffiths, R.E. & Ratnatunga, K. U. 1995, ApJ, 449, 23
- Ellis, R. E. 1997, ARA&A, 35, 389
- Elson, R.A.W., Santiago, B.X. & Gilmore G.F. 1996, New Astron., 1, 1
- Flynn, C., Gould, A., & Bahcall J. N. 1996, ApJ, 466, 55
- Fruchter, A. S., & Hook, R. N. 1996, in Proceedings from the 37th Herstmonceux Conference, “HST and the High Redshift Universe”
- Glazebrook, K., Ellis, R. S., Santiago, B. X. & Griffiths, R.E. 1995, MNRAS, 275, L19
- Gunn, J. E. & Stryker, L. L. 1983, ApJS, 52, 121
- Guzman, R., Gallego, J., KOO, D.C., Phillips, A.C., Lowenthal, J.D., Faber, S.M., Illingworth, G.D. & Vogt, N.P. 1997, ApJ, 489, 559
- Gwyn, S. D. J., & Hartwick, F. D. A. 1996, ApJ, 468, L77
- Haiman, Z., Madau, P. & Loeb, A. 1998, ApJ, submitted (astro-ph9805258)
- Hall, P. B., Osmer, P. S., Green, R. F., Porter, A. C., & Warren, S. J. 1996, ApJ, 462, 614

- Hartwick, F. D. A. & Schade, D. 1990, *ARA&A*, 28, 437
- Hasinger, G. 1998, *Astron. Nachr.*, 319, 37
- Jarvis, J. & Tyson, J. 1979, *SPIE Proc. on Instrumentation in Astronomy*, 172, 422
- Kawaler, S.D. 1996, *ApJ*, 467, 61
- Kennefick, J.D., Djorgovski, S.G., & de Carvalho, R.R. 1995, *AJ*, 110, 2553
- Kennefick, J.D., Osmer, P.S., Hall, P.B. & Green, R.F. 1997, *AJ*, 114, 2269
- Krist, J. 1993 in *Astronomical Data Analysis Software and Systems II*, ASP Conference Series 52
- Lanzetta, K.M., Yahil, A. & Fernandez-soto, A. 1996, *Nature*, 381, 759
- Lowenthal, J.D., Koo, D. C., Guzman, R., Gallego, J., Phillips, A. C., Faber, S.M., Vogt, N.P., Illingworth, G.D. & Gronwall, C., 1996, *ApJ*, 481, 673
- Madau, P., Ferguson, H.C., Dickinson, M.E., Giavalisco, M., Steidel, C.C. & Fruchter, A. 1996 *MNRAS*, 283, 1388
- Maoz, D. 1997, *ApJ*, 490, 35
- Mendez, R. A., Minniti D., de Marchi, G., Baker, A., Couch, W. J. 1996 *MNRAS*, 283, 666
- Metcalfe, N.; Shanks, T.; Campos, A.; Fong, R.; Gardner, J.P. 1996, *Nature*, 383, 236
- Miyaji, T., Connolly, A.J., Szalay, A.S. & Boldt, E. 1997, *A&A*, 323, 37
- Miralda-Escudè, J. 1998 *ApJ*501, 15
- Mobasher, B., Rowan-Robinson, M., Georgakakis, A. & Eaton, N. 1996 *MNRAS*, 282, 7
- Moffat, A.F.J. 1969, *A&A*, 3, 455
- Mutz, S., Windhorst, R.A., Schmidtke, P.C., Pascarella, S.M., Griffiths, R.E., Ratnatunga, K.U. et al. 1994, *ApJ*, 434, 55
- Newberg, H.J. & Yanny, B. 1997 *ApJS*, 113, 89
- Pettini, M., Steidel, C. C., Adelberger, K L., Kellogg, M., Dickinson, M., & Giavalisco, M. 1997, to appear in ‘ORIGINS’, ed. J.M. Shull, C.E., Woodward, & H. Thronson, ASP Conference Series (astro-ph/9708117)
- Phillips, A.C., Guzman, R., Gallego, J., Koo, D.C., Lowenthal, J.D., Vogt, N.P., Faber, S.M. & Illingworth, G.D. 1997, *ApJ*, 489, 543
- Roche, N., Ratnatunga, K.U., Griffiths, R.E., Im, M. & Neuschaefer, L. 1996, *MNRAS*, 282, 1247

- Sandage, A., & Luyten, W.J. 1967, ApJ, 148, 767
- Sandage, A., & Perelmuter, J. M. 1990, ApJ, 350, 481
- Sandage, A., & Vèron, P. 1965, ApJ, 142, 412
- Schmidt, M. 1970, ApJ, 1162, 371
- Schmidt, M. & Green R. 1983, ApJ, 269, 352
- Schmidt, M., Schneider, D. P. & Gunn, J. E. 1995, AJ, 110, 68
- Sawicki M.J., Lin H. & Yee H.K.C. 1997, AJ, 113, 1
- Steidel, C.C., Giavalisco, M., Dickinson, M. & Adelberger, K.L. 1996, AJ, 112, 352
- Siemiginowska, A., Kuhn, O., Elvis, M., Fiore, F., Mcdowell & J., Wilkes, B.J. 1995, ApJ, 454, 77
- Strecker, D. W., Erickson, E. F. & Whittenborn, F. C. 1979, ApJS, 41, 501
- Valdes, F. 1982, SPIE Proc. on Instrumentation in Astronomy, 331, 465
- Van den Bergh, S., Abraham, R.G., Ellis, R.S., Tanvir, Santiago, B.X. & Glazebrook, K.G. 1996, AJ, 112,359
- Warren, S. J., Hewett, P. C., Irwin, M. J., & Osmer, P.S. 1991, ApJS, 76 ,1
- Warren, S. J., Hewett, P. C., & Osmer, P.S. 1994, ApJS, 76 ,1
- Weir, N., Fayyad, U. M., Djorgovski, S. G., & Roden, J. 1995, PASP, 107, 1243
- Wilkes, B.J. 1986, MNRAS, 218, 331
- Williams, R. E., et al. (the HDF Team) 1996, AJ, 112, 1335
- Zepf, S.E., Moustakas L.A. & Davis, M. 1997, ApJ, 474, 1

Table 1. Point Source Completeness for the HDF Crude Combine Images[†]

Filter	Chip 2		Chip 3		Chip 4	
	50%	90%	50%	90%	50%	90%
U_{300}	26.9	26.3	26.8	26.2	26.9	26.2
B_{450}	28.9	28.0	28.7	28.0	28.8	28.1
V_{606}	29.1	27.7	29.2	28.0	29.0	27.6
I_{814}	28.2	26.8	28.2	26.8	28.1	26.8

[†]All magnitudes are in the Vega magnitude system.

Table 2. Compact Objects in the Hubble Deep Field[†]

ID	Chip	RA	Dec	X	Y	U_{300}	B_{450}	V_{606}	I_{814}	Δ^\ddagger		
		(12^h)	(62°)							F450W	F606W	F814W
		m s	//			mag	mag	mag	mag			
0094	2	36 46.40	14 08.59	1757.76	569.62	25.99	26.98	26.82	26.40	0.23	0.28	0.34
0129	2	36 47.65	14 05.78	1605.15	741.18	26.49	27.36	26.72	25.61	0.41	0.27	0.25
0134	2	36 47.15	14 15.92	1873.48	763.50	24.38	25.89	25.95	25.38	0.09	0.11	0.15
0212	2	36 50.14	14 10.40	1534.37	1188.69	26.30	27.05	26.95	26.67	0.36	0.35	0.47
0258	2	36 51.72	14 07.27	1350.77	1410.35	25.64	27.09	26.98	26.50	0.31	0.34	0.38
0273	2	36 54.20	13 35.87	453.45	1491.12	–	26.71	26.74	26.50	0.08	0.05	0.16
0276	2	36 54.73	13 28.01	235.68	1496.09	24.18	22.07	20.43	19.37	0.00	0.02	0.33
0341	2	36 52.82	14 32.05	1843.07	1836.59	23.83	22.42	21.69	20.82	0.00	0.00	0.00
0357	2	36 55.53	13 58.73	885.38	1934.88	25.51	26.99	26.92	26.75	0.18	0.23	0.53
0563	2	36 50.10	13 58.20	1257.46	1057.56	–	27.41	26.81	26.30	0.23	0.07	0.29
0598	2	36 51.64	13 47.40	900.36	1195.42	–	27.98	26.47	25.19	0.18	0.04	0.05
0661	2	36 53.12	13 46.23	768.32	1422.07	–	27.74	26.88	26.26	0.43	0.22	0.29
0710	2	36 54.00	13 51.61	829.84	1617.34	–	26.84	26.98	26.51	0.12	0.10	0.27
1379	3	36 56.53	13 27.41	1797.59	190.28	25.69	26.61	26.45	25.69	0.23	0.23	0.27
1429	3	36 53.67	13 08.25	1144.76	431.53	25.48	23.57	22.18	21.32	0.00	0.00	0.00
1477	3	36 52.97	12 56.76	918.34	647.86	25.51	26.95	26.41	25.42	0.21	0.24	0.17
1495	3	36 52.25	12 49.39	729.00	767.42	25.45	26.98	26.59	25.62	0.31	0.32	0.33
1515	3	36 58.56	13 05.48	1905.62	837.85	26.35	26.57	26.39	25.86	0.13	0.15	0.17
1548	3	36 54.05	12 45.58	980.10	980.82	25.71	26.47	24.67	22.73	0.03	0.03	0.01
1610	3	36 56.36	12 41.13	1306.91	1244.63	21.48	20.36	19.94	19.29	0.10	0.33	0.36
1627	3	36 51.44	12 20.74	310.88	1370.34	25.02	26.26	25.88	25.00	0.19	0.22	0.27
1670	3	36 55.63	12 23.63	1015.46	1597.39	–	26.71	26.50	26.11	0.15	0.11	0.15
1721	3	36 52.60	12 01.20	303.15	1902.13	–	26.77	26.31	26.01	0.73	0.02	0.01
1741	3	36 53.60	13 17.95	1231.60	203.56	–	26.57	26.28	25.94	0.19	0.18	0.22
1927	3	36 59.30	12 55.80	1927.68	1112.46	–	26.47	24.90	22.54	0.03	0.01	0.07
2086	3	36 55.38	12 13.40	872.46	1815.47	–	28.46	26.93	24.50	0.77	0.02	0.01
2103	3	36 52.56	12 01.70	301.32	1887.65	–	26.02	24.60	23.72	0.02	0.08	0.00
3027	4	36 48.62	12 07.80	1469.35	510.24	25.89	27.12	26.78	25.95	0.43	0.27	0.39
3112	4	36 46.58	11 57.16	1575.97	944.23	25.81	26.94	26.18	25.73	0.34	0.40	0.53
3121	4	36 45.41	12 13.57	1116.71	971.88	20.32	21.16	21.22	20.86	0.00	0.00	0.00
3134	4	36 43.79	12 32.09	577.30	1053.60	25.07	26.62	26.53	26.12	0.31	0.33	0.39
3148	4	36 45.78	11 50.55	1674.50	1136.57	26.12	26.57	26.14	25.73	0.26	0.30	0.33
3176	4	36 44.73	11 57.07	1451.73	1243.17	25.04	26.37	25.78	24.94	0.12	0.29	0.28
3177	4	36 42.86	12 27.87	611.79	1244.15	25.91	26.23	26.10	25.67	0.22	0.22	0.26
3221	4	36 44.60	11 39.45	1849.88	1437.03	–	26.86	26.66	26.31	0.23	0.29	0.20
3226	4	36 44.40	11 39.05	1846.01	1472.08	25.40	26.99	26.82	26.34	0.34	0.35	0.33
3227	4	36 42.90	12 03.46	1178.63	1477.11	–	27.11	26.88	26.55	0.34	0.33	0.45
3418	4	36 45.98	12 50.38	304.23	521.25	–	26.63	25.36	24.23	0.05	0.04	0.05
3421	4	36 46.76	12 37.06	666.06	524.04	–	25.86	24.14	22.32	0.02	0.05	0.04
3541	4	36 45.41	11 48.95	1685.95	1213.05	–	27.17	26.62	26.18	0.36	0.34	0.34
3595	4	36 40.88	12 34.00	334.51	1504.03	–	27.51	25.71	23.98	0.19	0.06	0.02

[†]Celestial coordinates are in epoch J2000. We used chip coordinates according to Williams et al. (1996).

[‡]This parameter represents the degree of deviation from the stellar profile of all the objects in the HDF selected as compact based on their measured I_0 value. Smaller numbers correspond to smaller deviations (see Section 4). The distribution of expected deviations given by our simulations is shown in Table 3.

Table 3. Variation of Δ as a function of magnitude[†]

Magnitude	$\Delta_{B_{450}}$		$\Delta_{V_{606}}$		$\Delta_{I_{814}}$	
	σ	3σ	σ	3σ	σ	3σ
23	0.022	0.066	0.021	0.063	0.011	0.034
24	0.021	0.064	0.022	0.065	0.018	0.053
25	0.035	0.104	0.023	0.068	0.020	0.060
26	0.055	0.166	0.035	0.106	0.058	0.174
27	0.090	0.271	0.076	0.228	0.255	0.764
28	0.428	1.285	0.309	0.927	0.440	1.321

[†]Defined in Section 4 as a measure of the departure of an object from the HDF PSF in the appropriate filter, Δ has been measured here for our simulated stars in order to provide a range of allowed variation as a function of magnitude. This range will be used to classify the 41 compact objects in the HDF.

Table 4. Quasar Candidates in the Hubble Deep Field

ID	Chip	$U_{300} - B_{450}$	$B_{450} - V_{606}$	$V_{606} - I_{814}$	Notes [†]
0094	2	-0.99	0.16	0.43	q (lz)
0212	2	-0.75	0.10	0.28	qs (lz)
0258	2	-1.45	0.11	0.48	qs (lz)
0563	2	–	0.60	0.51	qsf (hz)
1515	3	-0.22	0.18	0.53	qs (lz)
1670	3	–	0.21	0.39	qs (hz)
1721	3	–	0.46	0.30	qs (hz)
1741	3	–	0.30	0.34	qs (hz)

[†]All objects have $\Delta < 3\sigma$. Objects denoted by *q* have colors within the quasar locus and away from the stellar locus; objects denoted by *qs* have colors consistent with either quasars or stars. The designation *lz* is for objects which are UV bright, fall in the quasar locus in Figure 9, and are expected to have $z < 3$. Similarly, *hz* is for objects in the quasar locus in Figure 10 expected to have $z > 3$. However, for most of these objects there is a significant overlap with the stellar locus.

Table 5. Stars in the Hubble Deep Field

ID	Chip	$U_{300} - B_{450}$	$B_{450} - V_{606}$	$V_{606} - I_{814}$	Notes [†]
0134	2	-1.50	-0.06	0.57	s
0273	2	–	-0.03	0.25	s
0276 ^a	2	2.12	1.65	1.06	sf
0341 ^a	2	1.42	0.72	0.87	sf
0357	2	-1.49	0.07	0.17	scf
0598	2	–	1.52	1.28	scf
0710	2	–	-0.14	0.47	scf
1429 ^a	3	1.91	1.39	0.86	sf
1548	3	-0.76	1.80	1.92	sf
1610 ^a	3	1.12	0.43	0.65	sf
1927	3	–	1.57	2.37	sf
2086	3	–	1.53	2.43	scf
2103	3	–	1.41	0.89	sf
3121 ^a	4	-0.85	-0.06	0.36	sf
3221	4	–	0.20	0.35	scf
3418	4	–	1.27	1.12	sf
3421	4	–	1.71	1.83	sf
3595	4	–	1.80	1.73	sf

[†]Labeled as *s* are all the objects we have classified as stars in the HDF. Objects classified as stars by Flynn et al. (1996) are labeled as *f*. Objects denoted by *c* are stars from the FGB sample that have been re-examined.

^aSpectroscopically confirmed star. See Cohen et al. (1996) for details.

Table 6. Compact Galaxies in the Hubble Deep Field

ID	Chip	$U_{300} - B_{450}$	$B_{450} - V_{606}$	$V_{606} - I_{814}$	Notes [†]
0129	2	-0.87	0.64	1.12	g
0661	2	–	0.86	0.62	qs (hz)
1379	3	-0.92	0.16	0.76	q (lz)
1477	3	-1.44	0.54	1.00	q (lz)
1495	3	-1.53	0.40	0.96	q (lz)
1627	3	-1.24	0.38	0.88	q (lz)
3027	4	-1.23	0.34	0.83	q (lz)
3112	4	-1.13	0.77	0.45	g
3134	4	-1.55	0.09	0.41	q (lz)
3148	4	-0.45	0.43	0.41	q (lz) [‡]
3176	4	-1.33	0.59	0.84	q (lz)
3177	4	-0.32	0.13	0.42	q (lz)
3226	4	-1.58	0.17	0.48	q (lz)
3227	4	–	0.23	0.33	qs (hz)
3541	4	–	0.55	0.44	g

[†]All these objects are compact galaxies for which $\Delta > 3\sigma$. Objects denoted by *q* have colors within the quasar locus and away from the stellar locus; objects denoted by *qs* have colors consistent with either quasars or stars; objects denoted by *g* have colors not consistent with quasars. The designation *lz* and *hz* have the same meaning as in Table 4.

[‡]Falls within the locus of low *z* quasars in Figure 9 but is on the stellar locus in Figure 10.

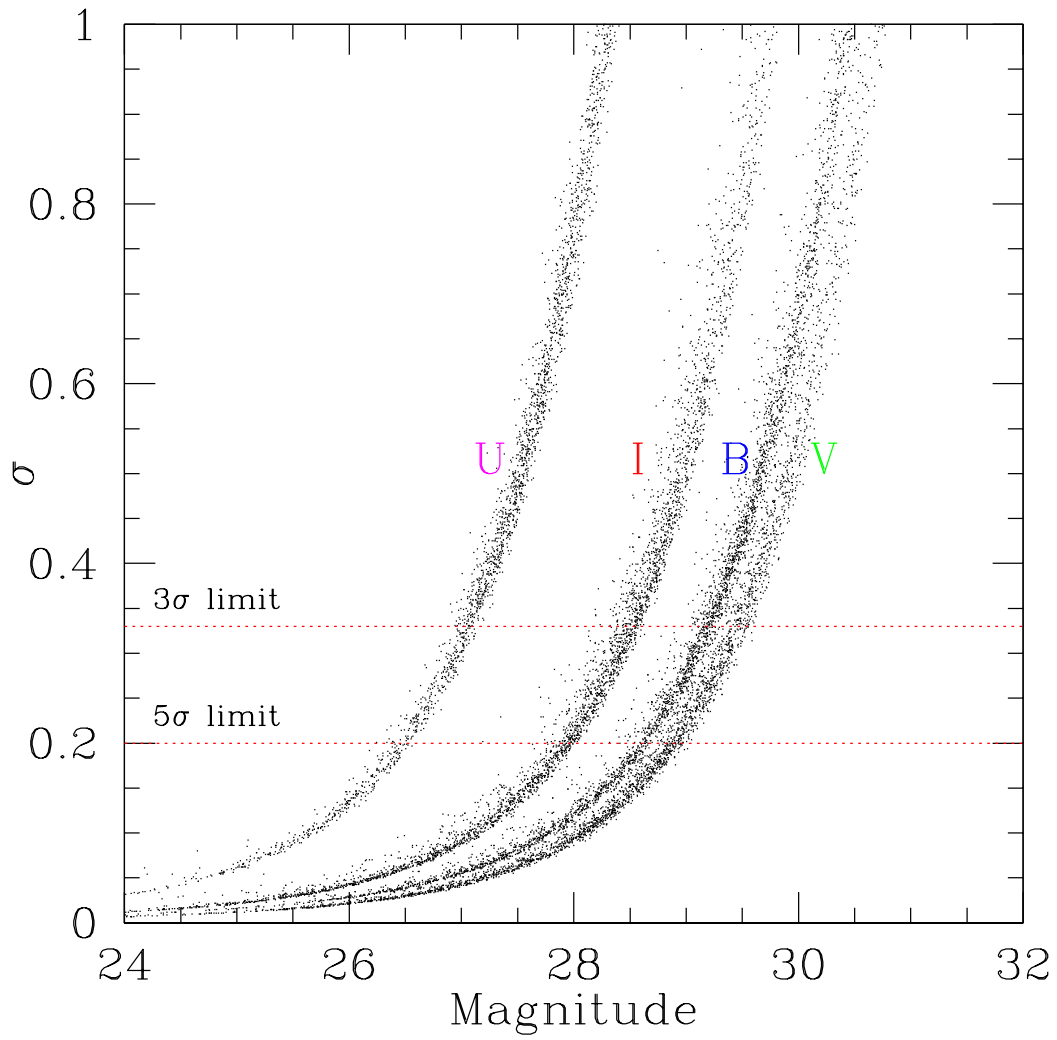


Fig. 1.— Photometric error as a function of magnitude in all the HDF filters as computed by IRAS/PHOT for all the objects in the Hubble Deep Field. The dotted lines represent the 3 and 5 σ magnitude limits.

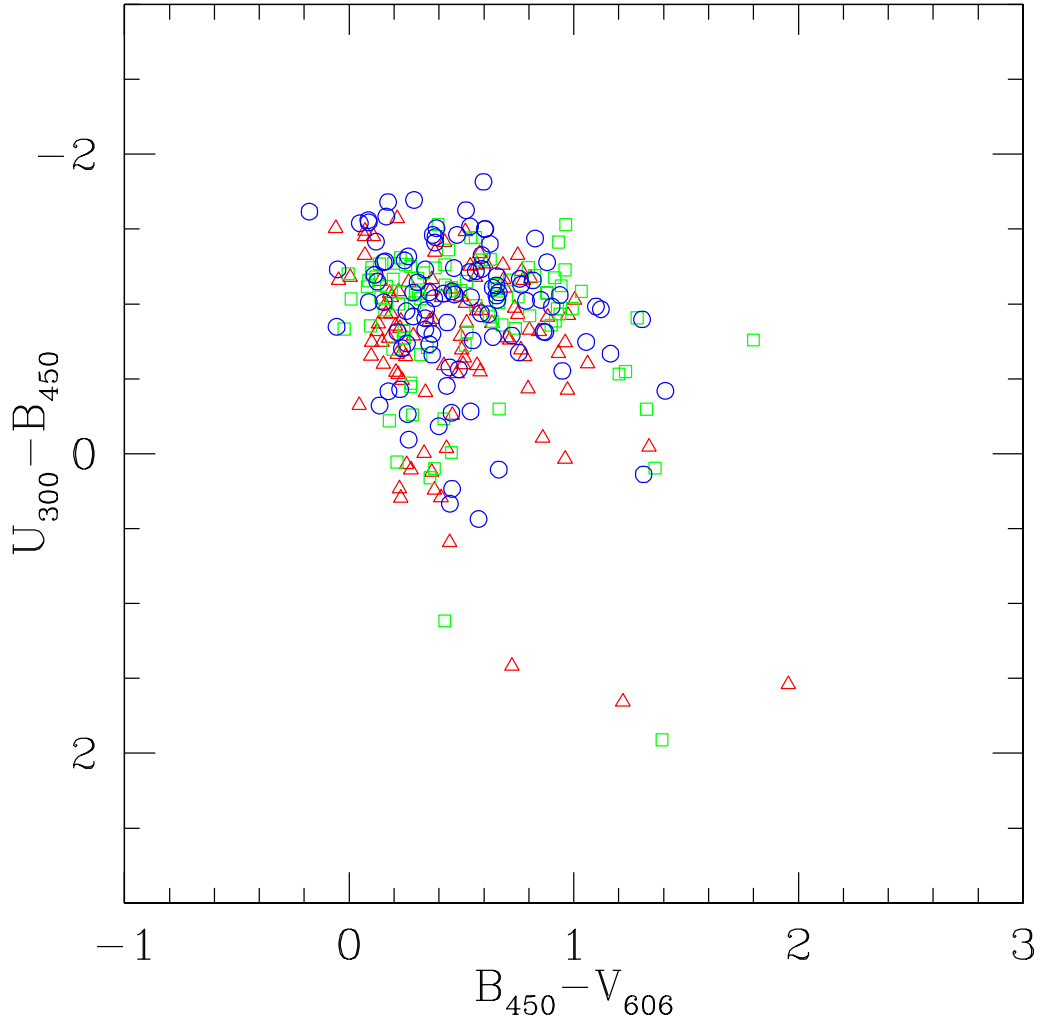


Fig. 2.— $(U_{300} - B_{450})/(B_{450} - V_{606})$ color-color diagram of all the objects in the HDF with a 5σ detection in all four bands. Open triangles represent sources in Chip 2, squares in Chip 3 and circles in Chip 4 respectively. The lack of a red population of objects is evident. Most of the objects have $-1.8 < (U_{300} - B_{450}) < 0$ and $0 < (B_{450} - V_{606}) < 1$. From our detailed analysis of the morphology of the bluest objects, we concluded that the blue sources that dominate the counts are likely to be regions of intense star formation rather than be of stellar origin.

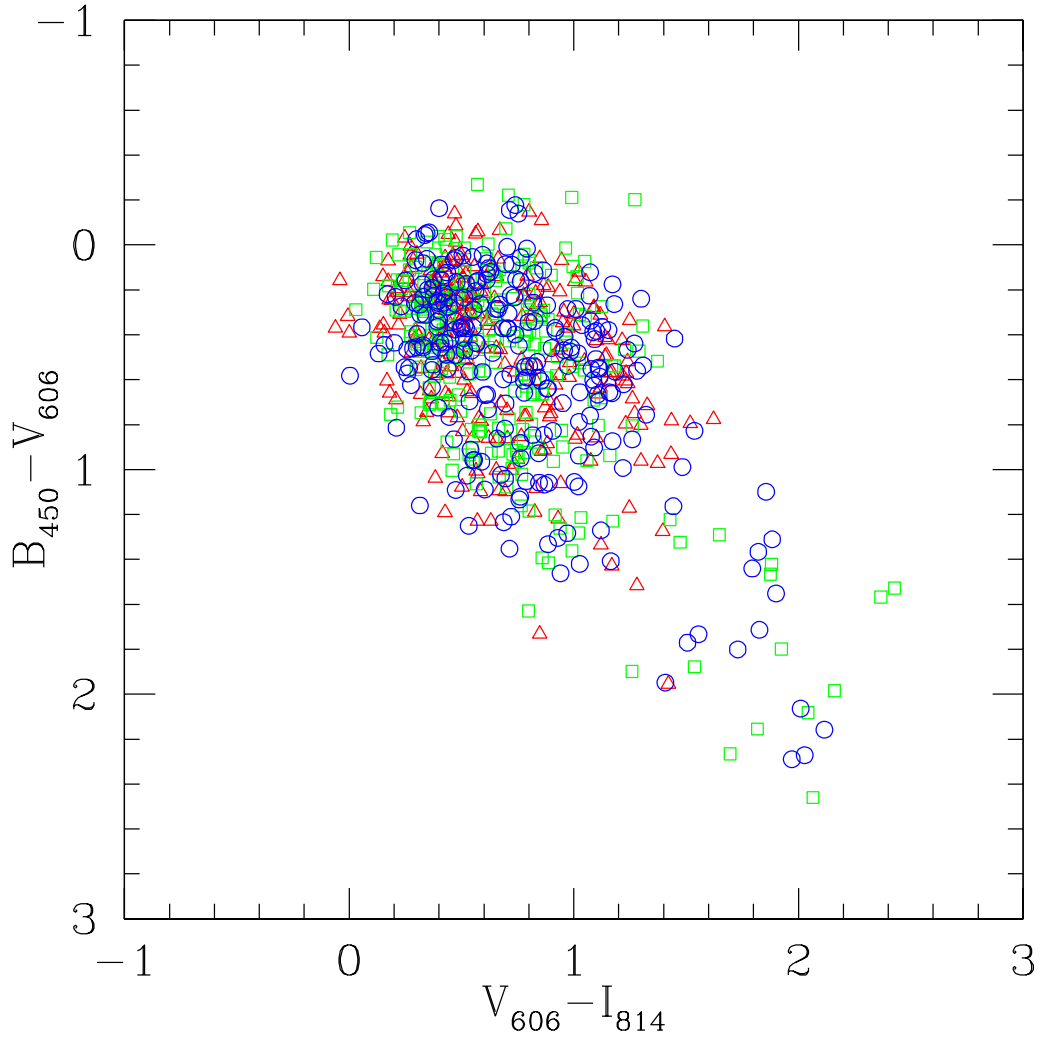


Fig. 3.— $(B_{450} - V_{606})/(V_{606} - I_{814})$ color-color diagram of all the objects in the HDF with a 5σ detection in all four bands. Open triangles represent sources in Chip 2, squares in Chip 3 and circles in Chip 4. The dominance of the blue population of objects is evident. The bulk of the objects have $-0.1 < (B_{450} - V_{606}) < 1.2$ and $0.2 < (V_{606} - I_{814}) < 1.3$. Our morphological analysis excludes a stellar origin for the great majority of this blue population.

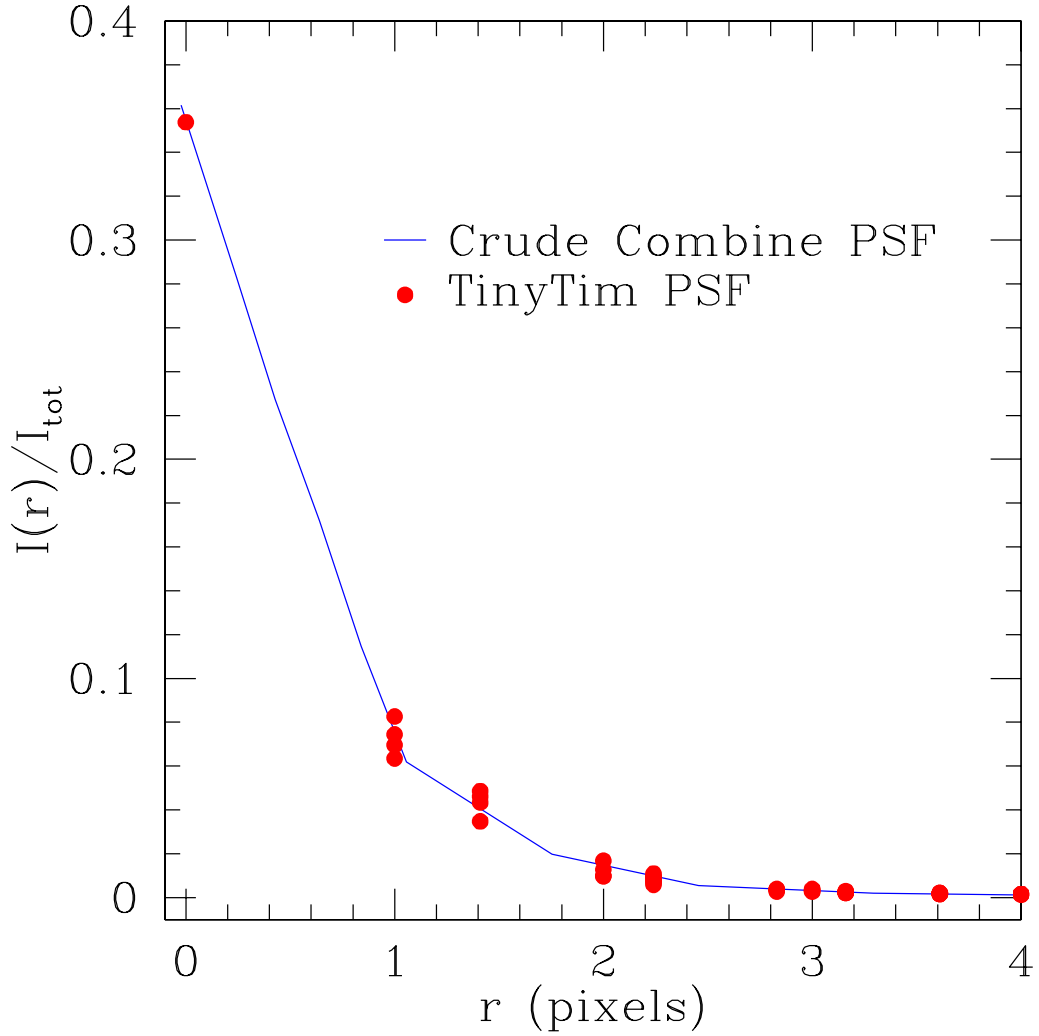


Fig. 4.— The crude combine PSF template used for Chip 4 in the I_{814} filter. Shown is the distance in pixels from the center of the template against the fraction of light falling on that pixel. The flux has been normalized to the total flux within a 4 pixel radius aperture. The WFPC2 undersampling is evident. The filled circles represent the PSF in the I_{814} filter generated by TinyTim that was used as a comparison to that of the actual crude combine images. As clearly shown, TinyTim implicitly makes the assumption that the source is always centered on the central pixel. Real sources will be randomly positioned with respect to the central pixel and hence produce a PSF that samples a wider range of distances from the center. A separate template for each chip and filter was used to determine the completeness of the dataset to point sources.

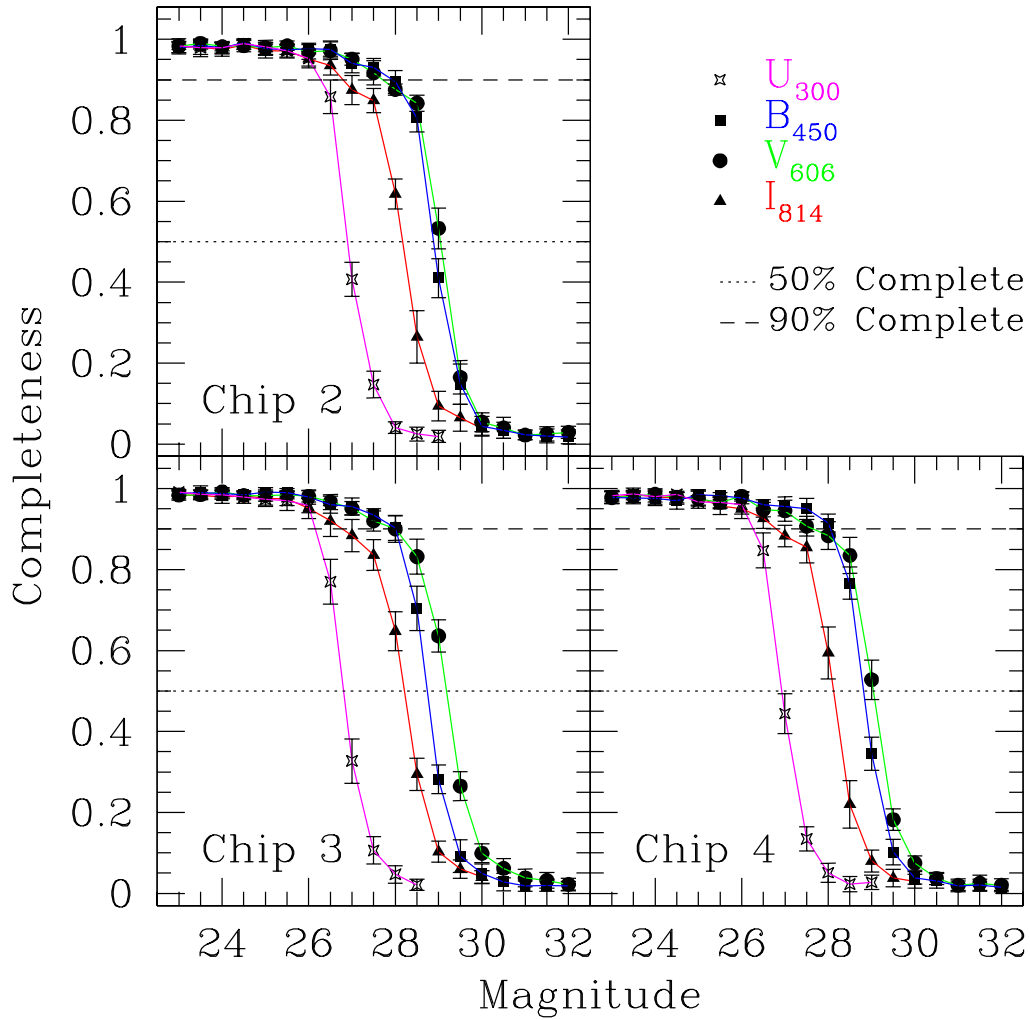


Fig. 5.— Completeness estimates for point sources in the Crude Combine images of the Hubble Deep Field. Shown is the fraction of added template point sources that were recovered as a function of magnitude. The simulations were run 10 times each and the error bars represent a 1σ spread around the mean value. Notice the slow linear decline before the sharp cutoff at the detection threshold. This change in behavior occurs at the $\sim 90\%$ completeness level. The plots are arranged as the actual WFPC2 chips on board Hubble, Chip 2 being on the top left corner, Chip 3 on the bottom left and Chip 4 on the bottom right.

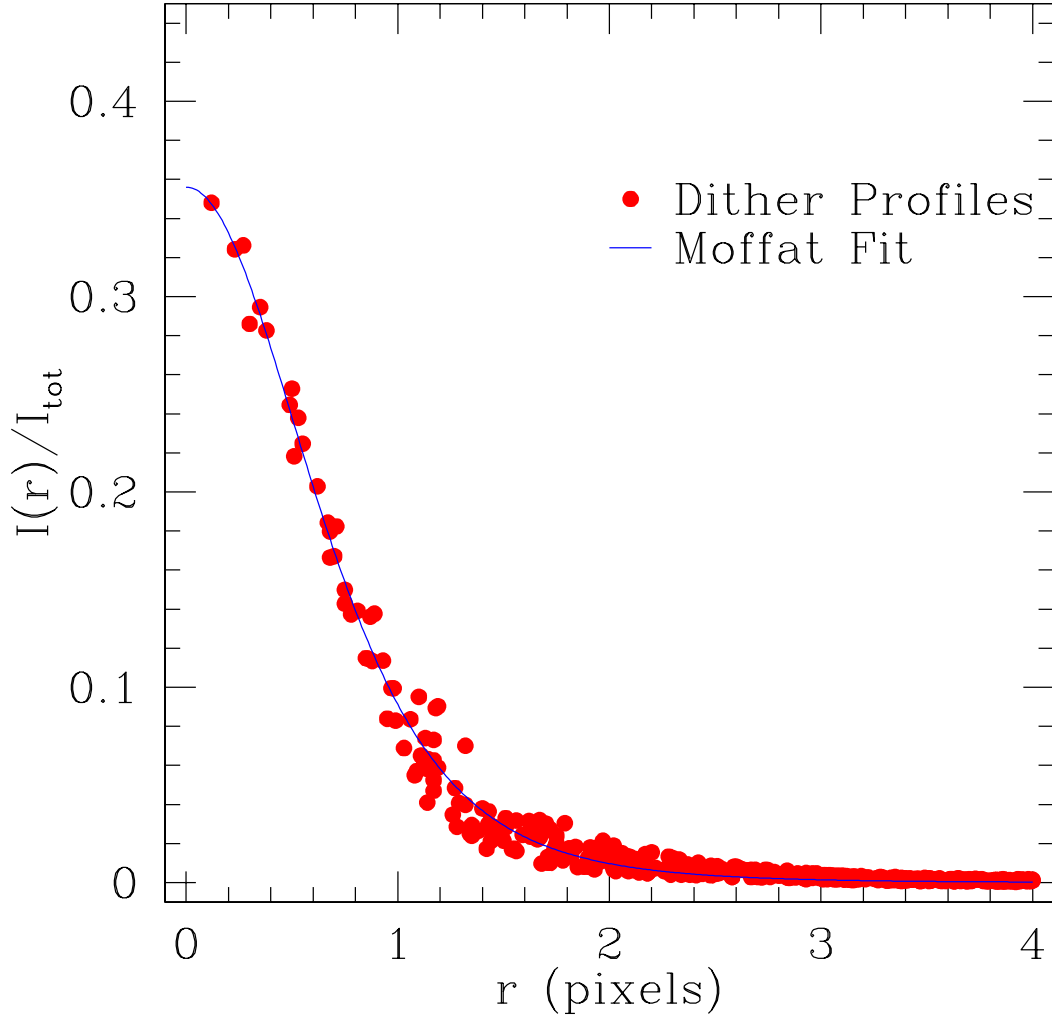


Fig. 6.— For classification purposes we need to be able to locate the center of the object with an accuracy of better than 0.1 pixels. This is accomplished by making use of the symmetry of the image about its center (see Flynn et al. 1996). By using single dither positions, we can effectively sample the objects’ radial profile well within the inner pixel, thereby overcoming the WFPC2 undersampling. The filled circles represent the 11 different V_{606} band dithers for a star in Chip 2. The solid line is a Moffat fit to the profile and it will be used as a “functional approximation” to the radial profile. This will allow for a systematic approach to object classification.

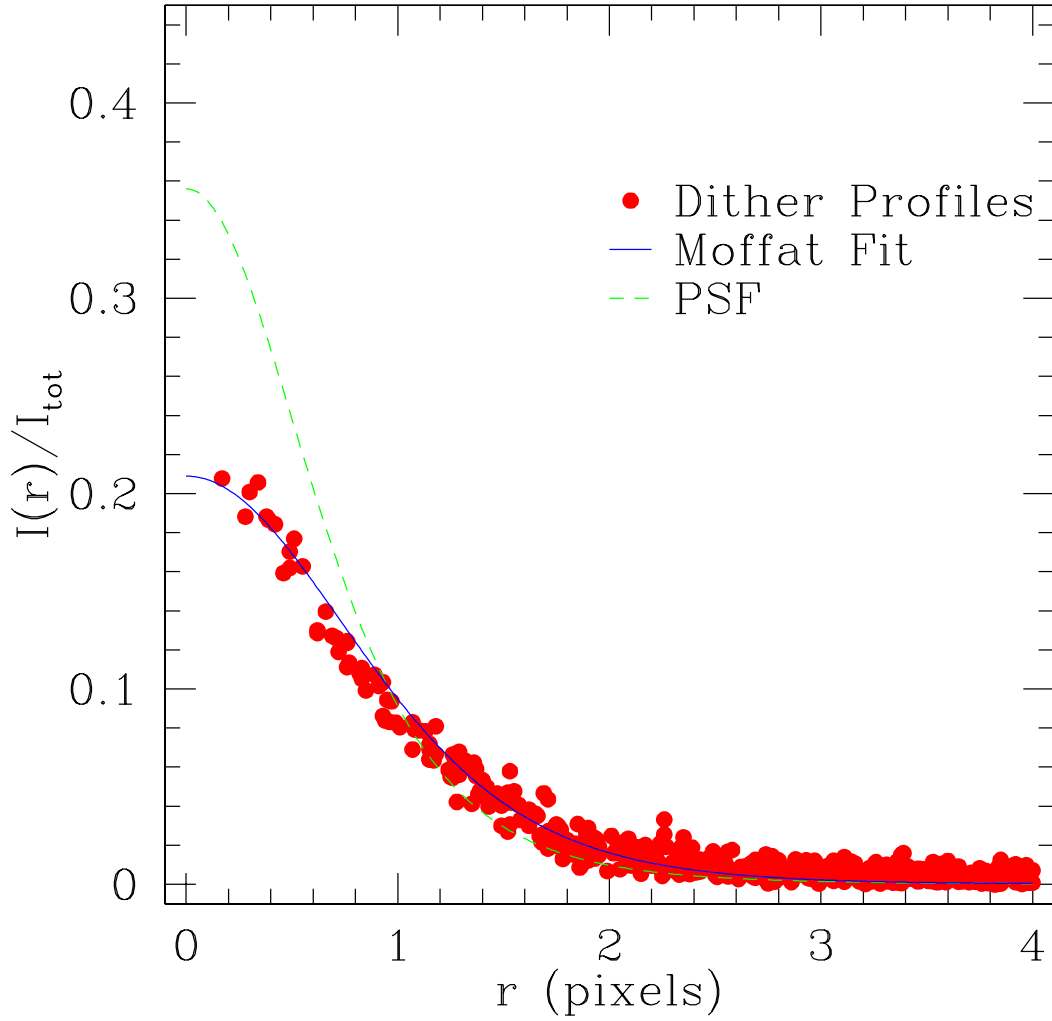


Fig. 7.— V_{606} band radial profile of a galaxy in Chip 4. The combined profile (filled circles) was obtained by adding together all the different radial profiles obtained from the 11 dither exposures. The solid line is a Moffat fit to the combined profile and the PSF is also shown for comparison. The central intensity parameter of the Moffat fit I_0 is indeed well suited for use as a star/galaxy separator.

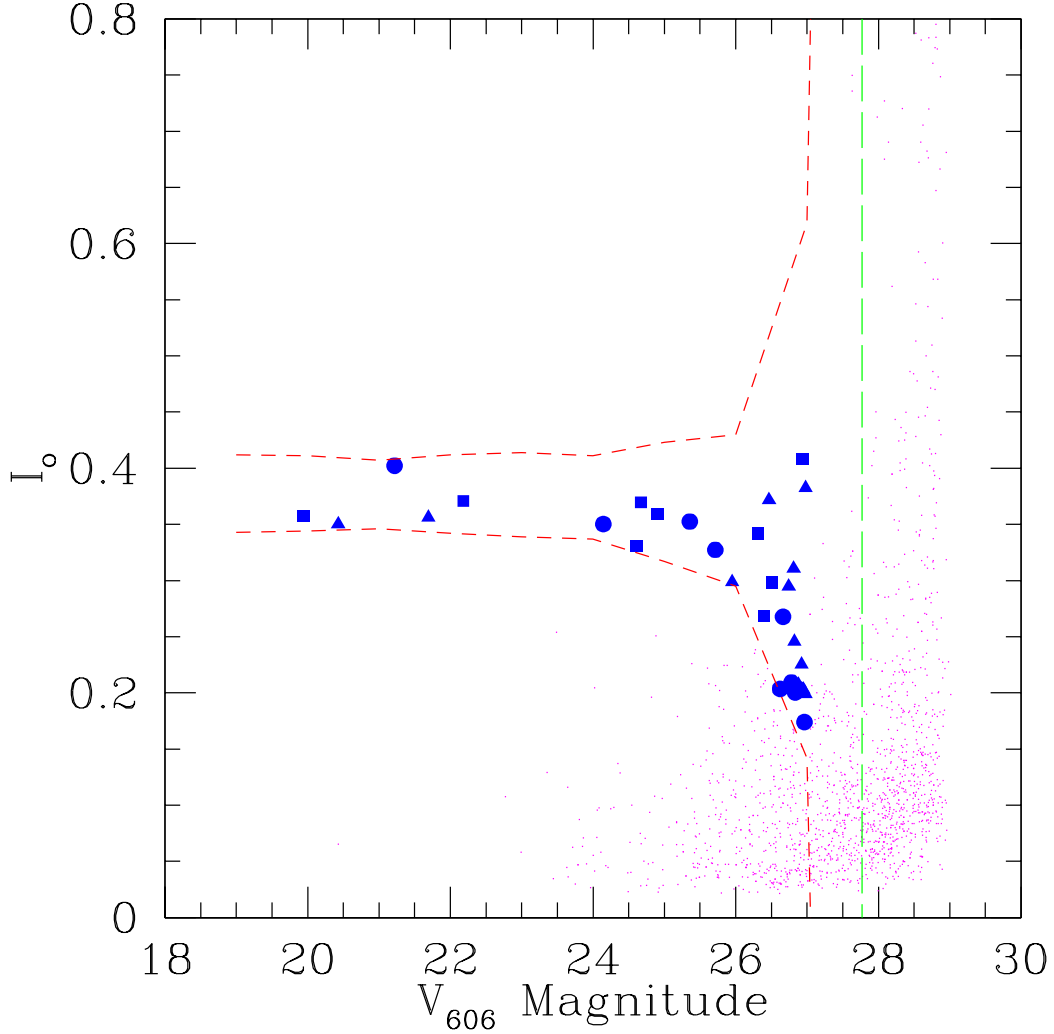


Fig. 8.— V_{606} stellar candidates in the HDF. The central intensity parameter I_0 is shown as a function of magnitude for all the objects in the HDF. Triangles represent sources in Chip 2, squares in Chip 3 and circles in Chip 4. Candidates are selected based on the expected variation of I_0 with magnitude given by our simulations. The area within the dotted lines represents the 95% confidence interval within which simulated stellar objects lie. As we approach the completeness limits of the dataset ($V_{606} = 27.8$, shown as a dashed line), I_0 becomes progressively unable to classify objects reliably.

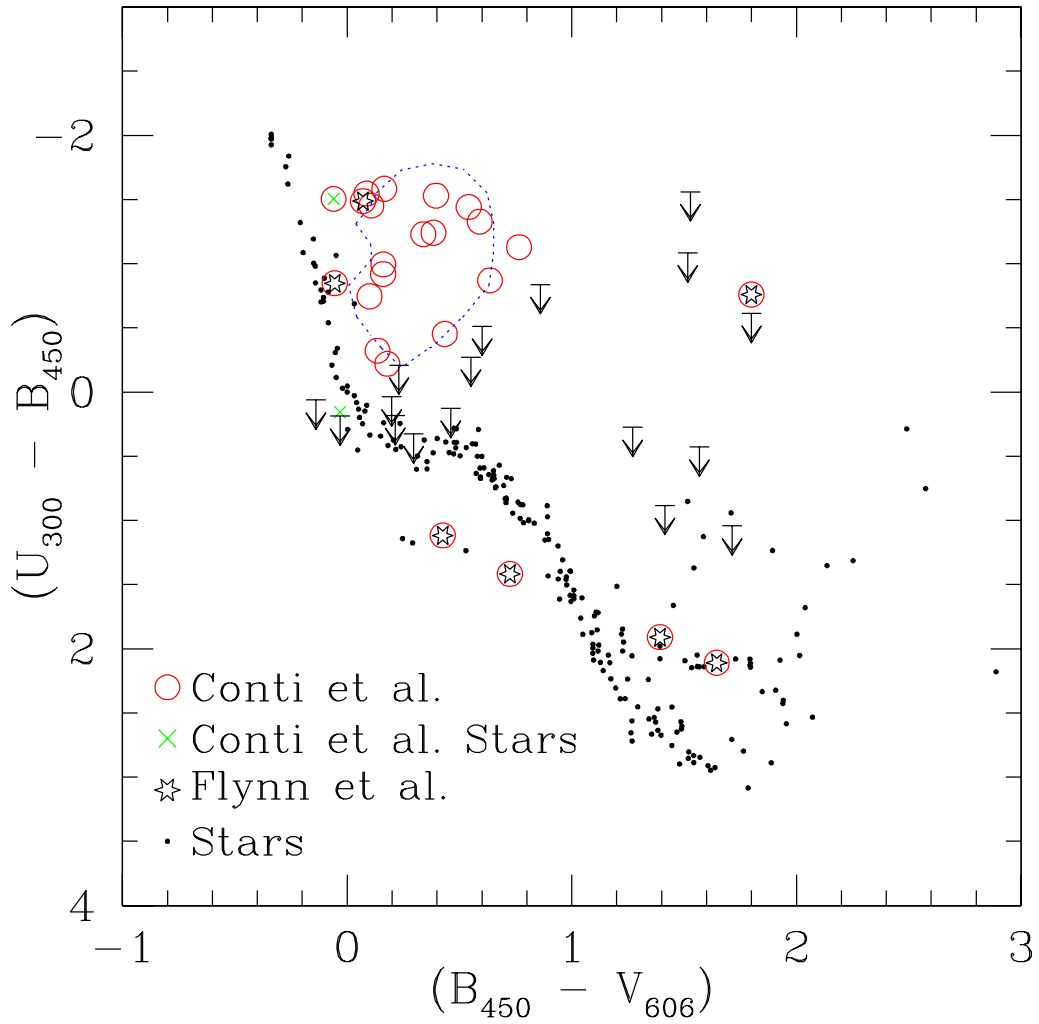


Fig. 9.— $(U_{300} - B_{450})/(B_{450} - V_{606})$ color-color diagram of the most compact sources in the HDF (shown as open circles). Objects classified as stars by Flynn et al. 1996 are shown as open stars, while new star candidates are shown as crosses. Filled circles represent stars from the Bruzual-Persson-Gunn-Stryker spectrophotometric atlas and are plotted to outline the stellar locus. The contour outlines our simulated low redshifts ($z < 2.2$) quasar colors. The contour encloses 99% our models. Limiting colors are also shown for those objects that do not have a U_{300} detection. Table 4 lists the main properties of our quasar candidates.

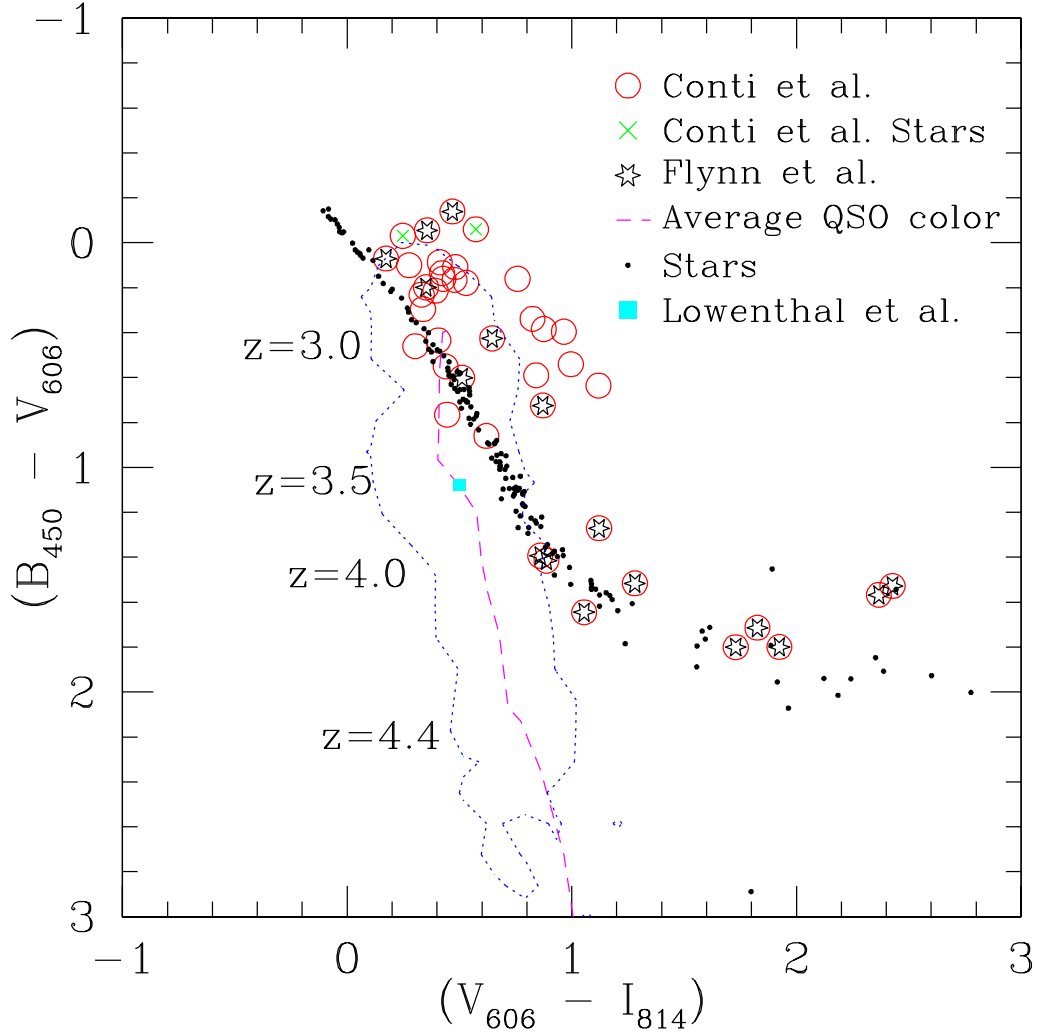


Fig. 10.— $(B_{450} - V_{606})/(V_{606} - I_{814})$ color-color diagram of the most compact sources in the HDF (shown as open circles). Objects classified as stars by Flynn et al. 1996 are shown as open stars, while new star candidates are shown as crosses. Filled circles represent stars from the Bruzual-Persson-Gunn-Stryker spectrophotometric atlas and are plotted to outline the stellar locus. The contour contains 99% of our high redshifts ($z > 3$) model quasars. The dashed line shows the average quasars color as a function of redshift. Also shown as a filled square is a known emission-line galaxy with $z = 3.368$ (Lowenthal et al. 1996) which was independently recovered as a relatively bright compact object during the early development stage of the classification algorithm.